Fast H isotope and impurity mixing in ion-temperature-gradient turbulence

C. Bourdelle[1]**, Y. Camenen**[2]**, J. Citrin**[3]**, M. Marin**[3]**, F.J. Casson**[4]**, F. Koechl**[4]**, M. Maslov**[4] **and The JET Contributors**[a]

[1] CEA, IRFM, F-13108 Saint-Paul-lez-Durance, France
[2] CNRS, Aix-Marseille Univ., PIIM UMR7345, Marseille, France
[3] DIFFER—Dutch Institute for Fundamental Energy Research, De Zaale 20, 5612 AJ Eindhoven, Netherlands
[4] CCFE, Culham Science Centre, Abingdon, Oxon, OX14 3DB, United Kingdom of Great Britain and Northern Ireland

E-mail: clarisse.bourdelle@cea.fr

Abstract

In ion-temperature-gradient (ITG) driven turbulence, the resonance condition leads to ion particle turbulent transport coefficients significantly larger than electron particle turbulent transport coefficients. This is shown in nonlinear gyrokinetic simulations and explained by an analytical quasilinear model. It is then illustrated by JETTO-QuaLiKiz integrated modelling. Large ion particle transport coefficients implies that the ion density profiles are uncorrelated to the corresponding ion source, allowing peaked isotope density profiles even in the absence of core source. This also implies no strong core accumulation of He ash. Furthermore, the relaxation time of the individual ion profiles in a multi-species plasma can be significantly faster than the total density profile relaxation time which is constrained by the electrons. This leads to fast isotope mixing and fast impurity transport in ITG regimes. In trapped-electron-mode (TEM) turbulence, in presence of electron heating about twice the ion heating, the situation is the inverse: ion particle turbulent transport coefficients are smaller than their electron counterpart.

Keywords: tokamak, turbulence, isotope, particle transport, impurity

(Some figures may appear in colour only in the online journal)

1. Introduction

Particle transport in tokamak plasmas, for electrons and light ions, is dominated by turbulent processes. The degree of density peaking in tokamaks depends strongly on turbulence regime, which impacts the convective velocity direction [1, 2]. For a 2-species plasma, the ion and electron density profiles are identical through quasineutrality. However, in a multi-ion plasma, additional complexity is introduced, with increased freedom. Individual ion density profiles can differ. Additional dynamics come into play, where ion profiles may respond to transients at a timescale independently from the electrons, as long as total ambipolarity is maintained (ion mixing). Understanding these dynamics is of high relevance for critical questions in tokamak fusion reactor operation, such as DT fuelling, He ash removal, and impurity transport timescales for core radiation control.

Experimental evidence for fast isotope mixing has been observed. In trace tritium (T) experiments on TFTR [3], where tritium gas were puffed from the edge into deuterium neutral-beam fueled plasmas, the T profile peaked over 100 ms, for an energy confinement time of 160 ms. In similar trace T at JET, the T profile is also observed to peak in the center with ratios of D_T/χ_{eff} varying between 0.3 and 2 [4]. Recent analysis of JET mixed isotope (H/D) experiments has shown that the density peaking of H and D isotopes are similar, and independent

of the relative location of H and D core and edge sources, both with D pellet in H plasmas [5] and with D-NBI in H plasmas [6]. In this latest case, D_i of H and D are above $2 \times \chi_{\text{eff}}$ [6]. Concerning trace helium (He) edge gas puff in D plasmas on DIII-D, it was found that, after 200 ms, the He density profile was similar to the peaked electron density profiles for various scenarios (L and H modes). The fast He core transport led to the conclusion that He ash removal is limited only by the recycling and pumping regime [7]. This conclusion is supported by linear and nonlinear gyrokinetic simulations, together with integrated modelling using a quasilinear transport model [8] where He diffusivities (D_{He}) of the order of the effective heat diffusivities χ_{eff} are found. In further gyrokinetic nonlinear simulations of mixed D-He plasma [9], significant $D_{\text{He}}/\chi_{\text{eff}}$ ratios were observed for a range of He normalized density gradients, hinting at fast relaxation times for He transients, although this was not specifically discussed. Concerning impurity transport, Si laser-blow-off experiments at AUG [10, 11] showed large anomalous impurity diffusion coefficients, with $D_{\text{Si}} \geqslant \chi_{\text{eff}}$, extending inwards to the plasma centre with on-axis electron heating. Further laser-blow-off experiments at JET, Tore-Supra and Alcator C-Mod also measured short impurity confinement times, significantly lower than the energy confinement time [12, 13].

The above experimental evidence points to the ubiquitousness of large ion transport coefficients. In this work, we show that despite the ambipolarity of the particle fluxes, the diffusive and convective ion coefficients are indeed predicted to be significantly larger from those of electrons in ion-temperature-gradient (ITG) driven turbulence. Therefore, for multiple-ion plasmas, the ion density profiles are less sensitive to the ion particle sources. From the basic transport equations, this can be seen from the following:

In a single-ion plasma, the ambipolarity constraint is cast as:

$$\Gamma_e = Z_i \Gamma_i. \tag{1}$$

Where Γ_e (resp. Γ_i) is the electron (resp. ion) particle flux, and Z_i the ion charge number. The particle fluxes are decomposed into diffusive (D_e, D_i) and convective (V_e, V_i) components:

$$\Gamma_e = -D_e \frac{\partial n_e}{\partial r} + V_e n_e \tag{2}$$

$$\Gamma_i = -D_i \frac{\partial n_i}{\partial r} + V_i n_i. \tag{3}$$

Even if $D_i \gg D_e$ and $|V_i| \gg |V_e|$, ambipolarity can still be respected, for example by a large outward ion diffusion counterbalanced by a large ion inward convective velocity (pinch). In a single-ion plasma the time-scale for relaxation of the core density profile (identical for ions and electrons) is set by the slower dynamics, of the ions or of the electrons.

However, in multiple-ion plasmas, there is more freedom in the ambipolarity constraint:

$$\Gamma_e = \sum_i Z_i \Gamma_i. \tag{4}$$

The individual ion fluxes are not tied to the electron flux. Ion density profile transients can thus relax at a timescale different

Table 1. Summary of the input parameters (main species only) for the ITG1 and TEM1 cases.

Case	$\frac{r}{R}$	q	$\hat{s}$	$\frac{R}{L_{T_e}}$	$\frac{R}{L_{n_e}}$	$\frac{R}{L_{T_i}}$	$\frac{R}{L_{n_i}}$	$\frac{T_e}{T_i}$
ITG1	0.1667	2	1	9	3	9	3	1
TEM1	0.1667	2	1	9	3	0	3	1

from the electron particle confinement time. As will be shown for ITG dominated turbulence, large ion transport coefficients ($D_i > D_e$ and $|V_i| > |V_e|$) lead to large transient ion fluxes relaxing at timescales comparable to the energy confinement time. Furthermore, these large ion transport coefficients reduce the dependence of the individual ion density profiles on the core sources, since the source term is reduced by a factor $\frac{1}{n_i D_i}$, as seen in the density transport equation:

$$\frac{\partial n_i}{\partial t} = -\frac{1}{V'} \frac{\partial}{\partial r} (V' \Gamma_i) + S_i \tag{5}$$

where S_i is the source term and V' the radial derivative of the plasma volume, which in stationary state implies:

$$-\frac{1}{n_i} \frac{\partial n_i}{\partial r} = -\frac{V_i}{D_i} + \frac{1}{V'} \int_0^r V' \frac{S_i}{n_i D_i} \, \mathrm{d}r. \tag{6}$$

These statements are supported in this paper through nonlinear simulations, analytical derivations and quasilinear transport models in fixed gradient standalone mode and used in conjunction with a flux driven integrated modelling approach.

Significant dependence of impurity transport to the ion to electron heat flux ratio (and hence turbulence regime) has been predicted [8, 14–18] by nonlinear and quasilinear gyrokinetic simulations.

However, to our knowledge, the ratios of ion to electron diffusivity and convectivity, D_i/D_e and $|V_i|/|V_e|$, and their dependence on turbulence regime, has never been pointed out. The novelty of this paper then lies in the following: (i) the prediction of separate particle confinement timescales for electrons and ions, which then is only evident for either multi-isotope plasmas, He ashes or impurities; (ii) integrated modelling simulations of multiple-isotope plasmas with a first-principle-based gyrokinetic turbulent transport model, with positive ramifications for isotope mixing.

In section 2, the dependence of D_i/D_e and $|V_i|/|V_e|$ on turbulence regime is shown for D in nonlinear fixed gradient gyrokinetic simulations performed by GKW [19]. In section 3 and in the appendix, using the quasilinear gyrokinetic derivation of turbulent fluxes [20], we explain why larger ion transport coefficients than electron transport coefficients are expected, for main ion and impurities, in the case of dominant ITG background turbulence, while the inverse holds for Trapped Electron Mode (TEM) turbulence. In section 4, the trends observed in the nonlinear simulations are replicated for D by quasilinear calculations using the QuaLiKiz transport model [20, 21]. Other H isotopes, He as well as impurity transport are also shown to have similar trends. Finally, in section 5, flux driven integrated modelling using QuaLiKiz within the JETTO integrated modelling suite [22, 23] is used for D and H plasmas to directly simulate the behaviour and
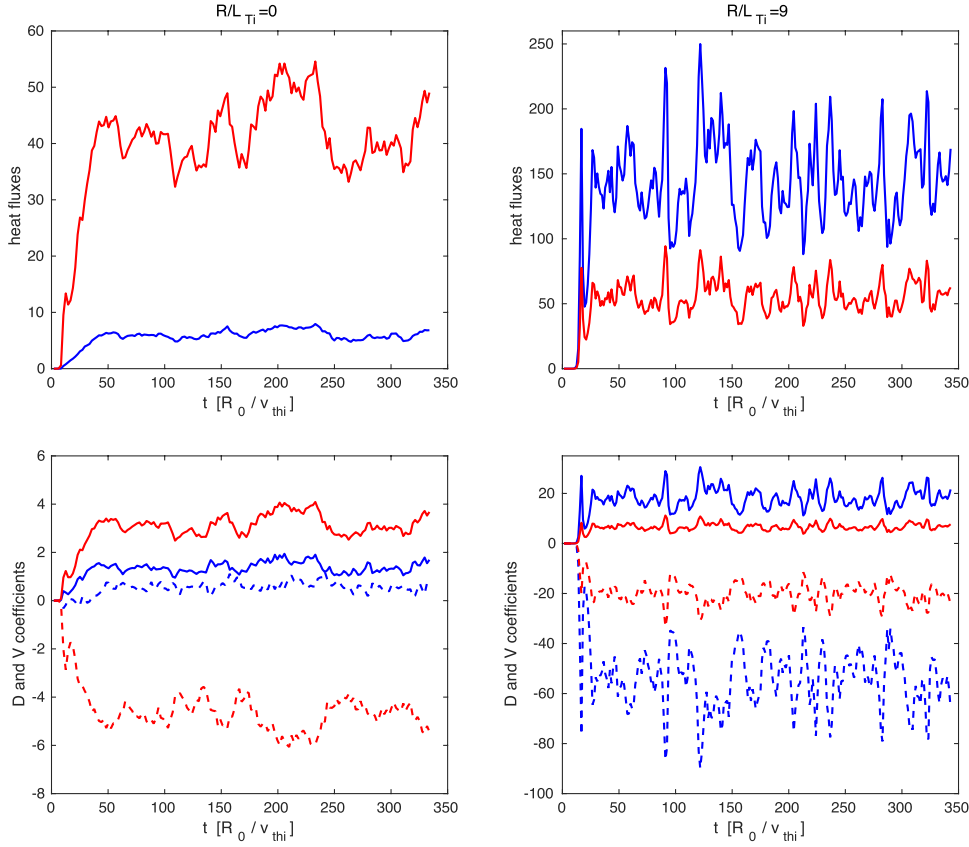
Figure 1. Top row: time evolution of the electron (red) and ion (blue) heat fluxes in the non-linear simulations at $R/L_{T_i} = 0$ (left column) and $R/L_{T_i} = 9$ (right column). Bottom row: corresponding particle diffusivity (full lines, D_e in red and D_i in blue) and particle pinch (dashed lines, V_e in red and V_i in blue). The heat fluxes are normalised to $nT\rho_*^2 v_{\mathrm{thi}}$, the diffusivities to $\rho_*^2 v_{\mathrm{thi}}R$ and the pinch coefficients to $\rho_*^2 v_{\mathrm{thi}}$.

timescales of multiple-ion particle transport. The conclusions are given in section 6.

2. Ion to electron particle diffusivity and convection in nonlinear GKW simulations

The ion and electron particle transport coefficients predicted by non-linear gyrokinetic simulations is compared for two reference cases, see table 1. The first one (ITG1) is the GA standard case [24] and is dominated by ITG turbulence. A second reference case (TEM1) dominated by TEM turbulence is obtained by setting the logarithmic ion temperature gradient R/L_{T_i} to zero in the GA standard case. The simulations are performed with the non-linear δf (gradient-driven) gyrokinetic code GKW [19] in its flux-tube mode (local approximation). To compute the ion and electron particle diffusivity and pinch, four kinetic species are included in the simulation, following [25]: two main species, deuterium and electrons, and two trace species with zero density and zero density gradient but otherwise identical to the main species. Alternatively (and equivalently), four non-trace species could be used provided their respective density gradient combine to a total of $R/L_n = 3$ for each species. The actual electron to deuterium mass ratio is used. No collisions, or rotation physics are included. The magnetic equilibrium is prescribed using the Miller parametrisation [26] for a circular plasma cross-section.

The 5D computational domain is discretised with $N_s = 32$ points in the direction parallel to the magnetic field (finite differences), $N_{k_\theta} \times N_{k_r} = 21 \times 339$ in the perpendicular plane (spectral decomposition) and $N_\mu \times N_{v_\parallel} = 16 \times 48$ points in velocity space (finite differences). Hyper-diffusive upwind dissipation is used for the derivatives along the magnetic field line or in the parallel velocity direction. The poloidal wave vectors range from $k_\theta \rho_i = 0$ to 1.2, with ρ_i the ion Larmor radius at the thermal velocity $v_{\mathrm{thi}} = \sqrt{2T_i/m_i}$ and the radial wave vectors from $k_r \rho_i = -10.73$ to 10.73.

The temporal evolution of the electron and ion heat fluxes is shown in the top row of figure 1. As expected, the electron heat flux is larger than the ion heat flux for the TEM dominated case, whereas the opposite is observed for the ITG dominated case. The particle diffusivities, D_e and D_i, and pinches, V_e and V_i, defined in equations (2)–(3) are computed by combining the main species and trace particle fluxes as follows:

$$D_s = \frac{1}{R/L_{n_s}^{\mathrm{main}}} \left[\frac{R\Gamma_s^{\mathrm{main}}}{n_s^{\mathrm{main}}} - \frac{R\Gamma_s^{\mathrm{trace}}}{n_s^{\mathrm{trace}}} \right] \qquad (7)$$

$$V_s = \frac{\Gamma_s^{\mathrm{trace}}}{n_s^{\mathrm{trace}}} \qquad (8)$$

where the subscript s represents the species label (e or i) and R is the reference major radius. Note that the values of D_s and V_s are 'local' values in the sense that, for the main species, they depend

Table 2. Time averaged values of the electron and ion heat flux, particle diffusivity and particle pinch obtained in the non-linear simulations at $R/L_{T_i} = 0$ and $R/L_{T_i} = 9$ (GA standard case). The heat fluxes are normalised to $nT\rho_*^2 v_{\text{thi}}$, the diffusivities to $\rho_*^2 v_{\text{thi}} R$ and the pinch coefficients to $\rho_*^2 v_{\text{thi}}$. $D_{\text{eff}} = D + L_n V$, and is the same for both species due to ambipolarity.

$\frac{R}{L_{T_i}}$	Q_e	Q_i	χ_{eff}	D_e	D_i	V_e	V_i	D_{eff}
0	42.0	6.1	5.3	3.2	1.4	-4.7	0.6	1.6
9	55.7	145.5	11.2	6.7	18.3	-20.0	-54.8	-0.01

on R/L_{n_s} (i.e. Γ_s is not linear in R/L_{n_s}). The temporal evolution of the particle transport coefficients is shown in the bottom row of figure 1. Interestingly, for the TEM dominated case: $D_e > D_i$ and $|V_e| > |V_i|$ whereas the opposite is found for the ITG dominated case: $D_i > D_e$ and $|V_i| > |V_e|$, see also table 2. As highlighted in the introduction, this difference in the electron and ion transport coefficients does not prevent the intrinsic ambipolarity of the particle fluxes ($\Gamma_e = \Gamma_i = 4.7569 \, n\rho_*^2 v_{\text{thi}}$ for the TEM1 case and $\Gamma_e = \Gamma_i = -0.0366 \, n\rho_*^2 v_{\text{thi}}$ for the ITG1 case). It has, however, important consequences for the response of the density profile to a core particle source or sink that will be discussed in section 5.

In table 2, the time average is performed from $t = 60R/v_{\text{thi}}$ to $t = 300R/v_{\text{thi}}$ and gyro-Bohm normalisation is used with $\rho_* = \rho_i/R$. The effective heat diffusivity is defined as $Q_e + Q_i = -n_e \chi_{\text{eff}}(\partial T_e/\partial r + \partial T_i/\partial r)$. As seen in table 2, for ITG1 $D_i > \chi_{\text{eff}} > D_e$, for TEM1 $D_i < D_e < \chi_{\text{eff}}$. The D_{eff} of both species is identical (due to ambipolarity), and it is interesting to note the extent to which the large diffusivities and inward pinch can cancel out, leading to a smaller D_{eff} and $D_{\text{eff}}/\chi_{\text{eff}} < 1$.

In the following section, a quasilinear derivation of the particle fluxes will explain why the ratio of D_i/D_e is larger in ITG dominated regime than in TEM dominated regime.

3. Quasilinear derivation of ion to electron particle transport coefficients

In this section, analytical expressions for the ion to electron particle transport coefficient are derived based on the quasilinear flux formulation, with additional approximations to allow focusing on the essential physics that sets the ion to electron D and V ratios: D_i/D_e and $|V_i|/|V_e|$.

The quasilinear particle flux derivation in a simplified quasilinear gyrokinetic limit is detailed in the appendix. This analytical limit allows to directly calculate, for a single mode, D_i/D_e, using equations (A.5) and (A.6) derived in the appendix for the particle flux carried by trapped and passing particles, respectively.

$$\frac{D_i}{D_e} = \frac{D_{ip} + D_{it}}{D_{ep} + D_{et}}$$

$$= \frac{\left\langle \dfrac{f_p}{\left(\bar{\omega}_k + \frac{2k_\theta \rho_0}{Z_i} v^2 - \frac{1}{q}\sqrt{\frac{2}{A_i}} v\right)^2 + \bar{\gamma}_k^2} + \dfrac{f_t}{\left(\bar{\omega}_k + \frac{k_\theta \rho_0}{Z_i} v^2\right)^2 + \bar{\gamma}_k^2} \right\rangle}{\left\langle \dfrac{f_p}{\left(\bar{\omega}_k - 2k_\theta \rho_0 v^2 - \frac{1}{q}\sqrt{\frac{2m_p}{m_e}} v\right)^2 + \bar{\gamma}_k^2} + \dfrac{f_t}{\left(\bar{\omega}_k - k_\theta \rho_0 v^2\right)^2 + \bar{\gamma}_k^2} \right\rangle}. \quad (9)$$
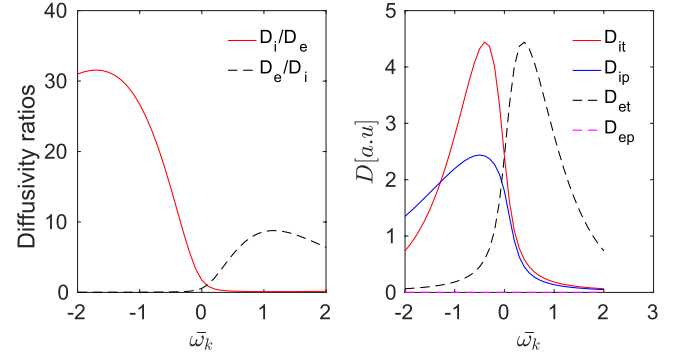

Figure 2. Ratios of D_i/D_e and D_e/D_i for a range of input frequencies (left panel), corresponding to a direct calculation of equation (9), with $\bar{\gamma} = 0.2$. The right panel shows the breakdown of the contribution to the diffusivities according to trapped and passing ions, and trapped and passing electrons. Note that the passing electron contribution is always negligible.

Here D_{sp} (resp. D_{st}) is the diffusion coefficient carried by the passing (resp. trapped) species s. $\bar{\omega}_k$ and $\bar{\gamma}_k$ are the mode frequency and growth rate at each wave vector k normalised by c_s/R. Note that by convention, positive (resp. negative) $\bar{\omega}_k$ means modes drifting in the electron (resp. ion) diamagnetic frequency. For the trapped particles, a resonance in the Lorentzian leading to large diffusivities, is only possible for modes drifting in the ion diamagnetic direction, $\bar{\omega}_k < 0$, for D_{it} and for modes drifting in the electron diamagnetic direction, $\bar{\omega}_k > 0$, for D_{et}. Concerning passing particles, the $\sqrt{m_p/m_e}$ in the electron parallel dynamics term means that only a narrow resonance occurs, such that the contribution of D_{ep} to D_e is negligible. We thus expect that $D_i/D_e > 1$ for Ion Temperature Gradient (ITG) modes with $\omega_k < 0$, and $D_i/D_e < 1$ for Trapped Electron Modes (TEM) with $\omega_k > 0$, as observed in the GKW nonlinear simulations, figure 1. The present analytical derivation, equation (9), is illustrated in figure 2, with $A_i = 2$ and $Z_i = 1$. The calculation is performed for a typical growth rate value of $\bar{\gamma} = 0.2$, $f_p = f_t$, a typical ion-scale mode wavevector of $k_\theta \rho_0 = 0.5$, and $q = 2$. $\bar{\omega}_k$ was scanned in both ion and electron diamagnetic directions. The exact value of the self-consistent growth rate (not calculated here) has little impact on the general dependence of D_i/D_e on the mode frequency. Note that the $D_i/D_e = 1$ location is not at $\bar{\omega}_k = 0$ due to non-negligible contributions of the passing ion flux in the $\bar{\omega}_k > 0$ region. This points to TEM modes having D_i/D_e closer to unity than ITG modes, a trend already evident in the nonlinear simulations in section 2, figure 1.

This dependence of D_i/D_e on the resonance condition is strongly related to the well known result that ion heat flux dominates electron heat flux for ITG dominated regimes, and electron heat flux is dominant for TEM regimes. Therefore the
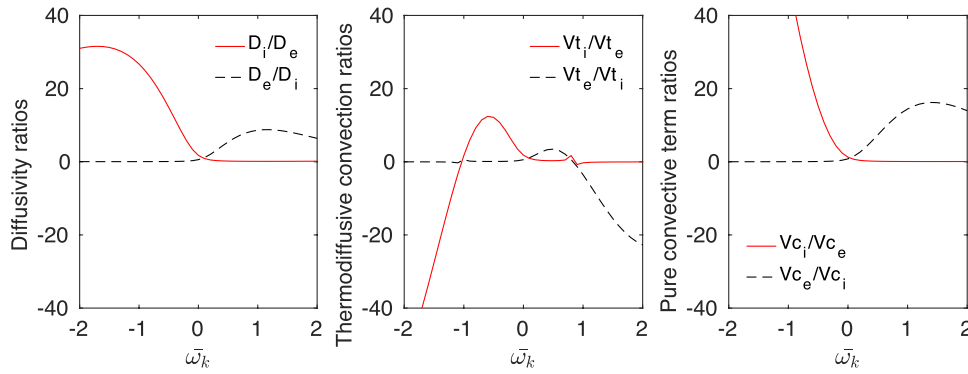
Figure 3. Left panel: ratios of D_i/D_e and D_e/D_i for a range of input frequencies as in figure 2. Central panel: ratios of $V_{t,i}/V_{t,e}$ and $V_{t,e}/V_{t,i}$ for a range of input frequencies. Right panel: ratios of $V_{c,i}/V_{c,e}$ and $V_{c,e}/V_{c,i}$ for a range of input frequencies.

parametric dependencies of D_i/D_e are expected to be similar to the one of Q_i/Q_e. The resonance condition was also shown to play a fundamental role in determining the ratio D_Z/chi_{eff}, in particular for heavy impurities [18].

Concerning the convection velocity ratios, integrations similar to equation (9) for the thermodiffusion ratio $V_{t,i}/V_{t,e}$ and the compressibility ratio $V_{c,i}/V_{c,e}$ are carried out (for more details on these particle convective velocity definition see [27]). In spite of the modified v dependences, one finds, as illustrated on figure 3, that both $|V_{t,i}/V_{t,e}|$ and $V_{c,i}/V_{c,e}$ share the same trend as D_i/D_e: >1 for ion modes and <1 for electron modes. We note that $V_{t,i}/V_{t,e}$ has lower absolute values compared to the other ratios, particularly in the range $\bar{\omega}_k < 1$. $V_{t,i}/V_{t,e}$ can also change sign, likely due to the $v^2 - \frac{3}{2}$ dependence in the numerator, and the dependence of the v resonance location on $\bar{\omega}_k$.

Finally, we discuss the mass and charge dependence of the D_i/D_e ratio. For A_i, the only dependence is a $\sqrt{A_i}$ dependence in the parallel dynamics term for the passing ions only, and hence the impact is expected to be weak. For ion (resp. electron) modes, higher Z_i narrows the width of the resonance, reducing the ion (resp. electron) particle diffusivity, see equation (9). We thus expect higher Z_i to decrease D_i/D_e for ion modes and to decrease D_e/D_i for electron modes. This is indeed observed in direct calculation (at $\bar{\omega}_k = \pm 1$), displayed in figure 4 and summarized in table 3. Note that while there is significant variation, the diffusivity ratio saturates at still high D_i/D_e at high Z_i for $\bar{\omega} = -1$. This indicates that we may expect fast impurity transport with respect to the electron transport in the ITG regime.

4. Parametric dependences of the ion to electron particle fluxes ratio in quasilinear QuaLiKiz simulations

Here we will focus on the particle transport fluxes using standalone QuaLiKiz. Situations where the dominant unstable modes are in the ion drift direction and in the electron direction are explored. The trend predicted in the previous section is recovered, the impact of the main ion mass/charge is explored as well as trace impurity transport dependences.
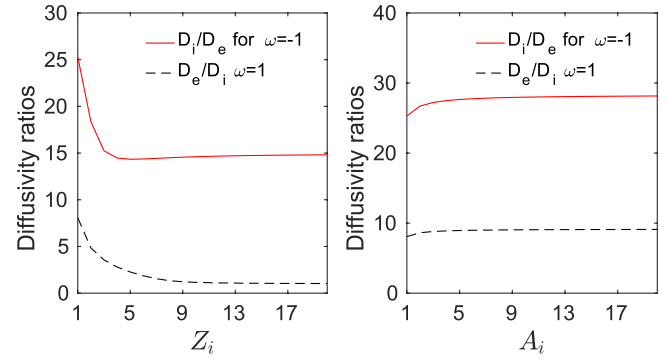

Figure 4. Ratio of D_i/D_e for a frequency in the ion diamagnetic direction ($\bar{\omega}_k < 0$), and D_e/D_i for a frequency in the electron direction ($\bar{\omega}_k > 0$), for a scan of ion charge (left panel) and ion mass (right panel).

Table 3. Impact of turbulence nature, Z_i, A_i on D_i/D_e.

	ITG dominated	TEM dominated
D_i/D_e	>1	<1
Larger Z_i	D_i/D_e decreases, then saturates at $D_i/D_e \gg 1$	D_i/D_e increases, then saturates at $D_i/D_e \sim 1$
Larger A_i	Weak impact on D_i/D_e	Weak impact on D_i/D_e

QuaLiKiz is run in stand-alone using 20 modes between $k_\theta \rho_s = 0.1$ and 2. QuaLiKiz uses a $s - \alpha$ equilibrium. The relative accuracy on 1D and 2D integrals is 10^{-4} and 2×10^{-3}, respectively. In QuaLiKiz, the D and V particle transport coefficients are calculated directly from the quasilinear flux decomposition [20].

4.1. Impact of the turbulence regime on the particle fluxes ratio

The normalized ion temperature gradient R/L_{T_i} is scanned from 0 to 12, while the other parameters are the ones of the GA standard case, see table 1, i.e. without collisions and without rotation. We note that QuaLiKiz is an eigenvalue gyrokinetic code and all the unstable modes are additively contributing to the quasilinear fluxes, more details can be found in [20]. For $R/L_{T_i} < 5$, only modes drifting in the electron diamagnetic direction (positive frequency in QuaLiKiz normalizations) are unstable, see figure 5. As expected, for this TEM dominated
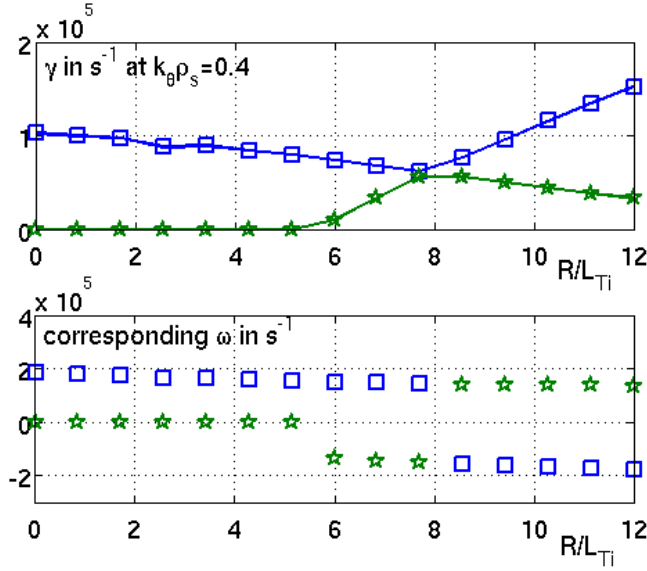
Figure 5. Upper figure: growth rate at $k_\theta \rho_s = 0.4$ for the two most unstable branches versus R/L_{T_i} (other parameters from GA standard case, see table 1). Lower figure: corresponding frequency versus R/L_{T_i}, when negative (resp. positive) the mode drifts in the ion (resp. electron) diamagnetic direction. Blue squares stand for the most unstable branch, green stars for the subdominant branch.
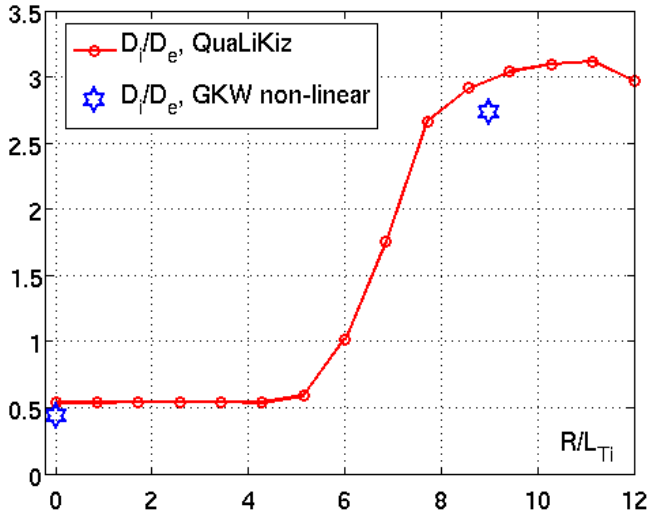

Figure 6. Ratio of ion to electron particle diffusivities versus R/L_{T_i} (other parameters from GA standard case, see table 1). The red circles are for QuaLiKiz ratios and the blue stars for GKW ratios as given in table 2.

regime, the ratio D_i/D_e stands well below one, see figure 6. For $5 < R/L_{T_i} < 8$, two unstable modes are co-existing, one in the ion drift direction (negative frequency) and one in the electron drift direction (positive frequency), see figure 5. In this region, although the most unstable mode is drifting in the electron drift direction, the destabilization of the ITG branch leads nonetheless to larger D_i/D_e as visible in figure 6. Finally, for $R/L_{T_i} > 8$, the ITG branch becomes dominant and the ratio D_i/D_e saturates to values much larger than unity, as expected.

The D_i/D_e ratios obtained in non-linear GKW simulations (see section 2) for the TEM1 case at $R/L_{T_i} = 0$ and the ITG1
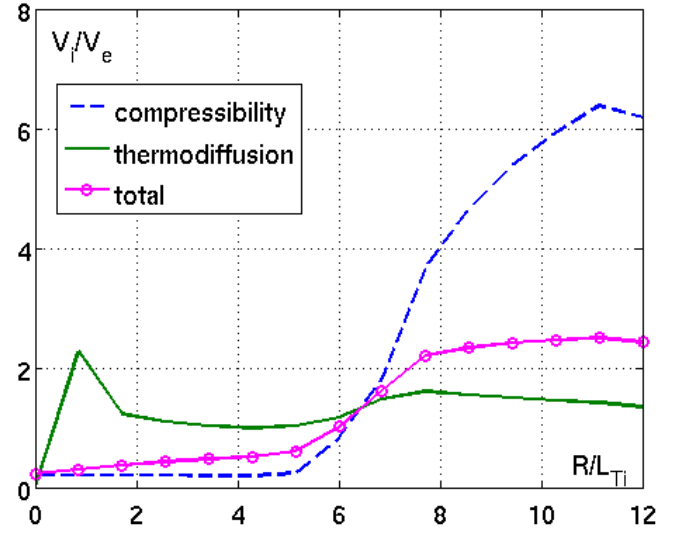

Figure 7. Ratio of ion to electron convective velocities, versus R/L_{T_i} (other parameters from GA standard case, see table 1). Magenta circles: ratio of the total convective velocities. Blue dashed lines: ratio of the compressibility components. Green full lines: ratio of the thermodiffusion components.
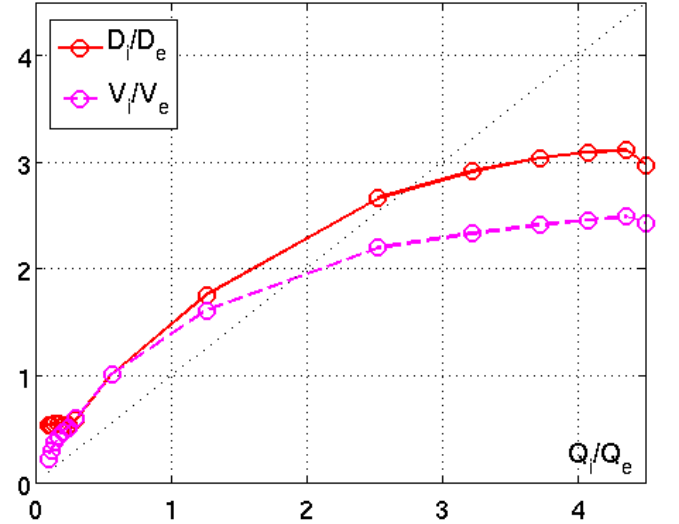

Figure 8. Ratio of ion to electron diffusivities and convective velocities versus Q_i/Q_e (other parameters from GA standard case, see table 1). Magenta dashed line circles: ratio of the total convective velocities. Red line and circles: ratio of the diffusivities.

case at $R/L_{T_i} = 9$ are added on figure 6. The quasi-linear estimates are very close to the non-linear values for these two cases.

The convection velocities are also plotted with respect to R/L_{T_i}. The overall trend for the total convective velocity ratio is similar to that of D_i/D_e, i.e. from below one in the TEM dominated regime to above one in the ITG dominated regime, see figure 7. Moreover, it is interesting to note that, as predicted by the analytical model (see figure 3), the thermodiffusion ratio $V_{t,i}/V_{t,e}$ has a weaker variation than the compressibility velocities ratio $V_{c,i}/V_{c,e}$ over the R/L_{T_i} scan, see figure 7. Note that in QuaLiKiz, the compressibility term accounts for both the turbulence equipartition (or curvature and ∇B compressibility) contribution and for the parallel
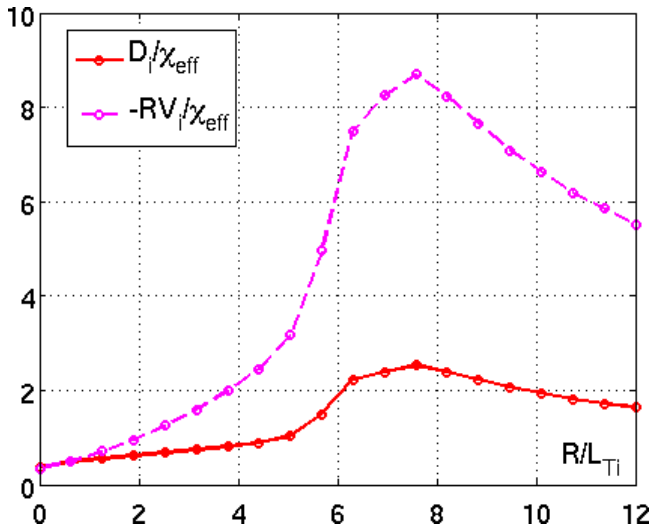
Figure 9. Ratio of the ion diffusivity and convective terms to χ_{eff}, versus R/L_{T_i} (other parameters from GA standard case, see table 1).

Figure 10. Ratio of ion to electron diffusivities, versus R/L_{T_i} (other parameters from GA standard case, see table 1). Red line and circles: collisionless case. Red line and dots: collisional case.

Figure 11. Ratio of ion to electron diffusivities, versus R/L_{T_i} for H, D, T and He without collisions (other parameters from GA standard case, see table 1). Magenta dashed line and smaller circles: H. Red line and circles: D. Darker red dot-dashed line and smaller circles: T. Blue line and squares: He.

compressibility contribution, for a review on particle transport see [27].

It is also interesting to note that the D_i/D_e ratio and the V_i/V_e ratio are strongly correlated to the ion to electron heat flux ratio, see figure 8. In particular, D_i/D_e is above one for $Q_i > Q_e/2$, on ion-scales, which is the case of most plasmas, including reactor-relevant alpha heated scenarios, where ion–electron heat exchange and radiation contribute to maintaining the heat flux ratio in an ITG regime [28–32].

When comparing the diffusive and convective contributions to the ion particle flux (respectively D_i and RV_i) to the total effective heat diffusivity χ_{eff} as often done in other modelling works [8, 9], one sees that it is mostly the convective contribution to the ion particle transport which is much larger than χ_{eff} in the ITG dominated regime, with an inward $|RV_i|$ up to 8 times χ_{eff}, while D_i is at most 2.5 times larger than χ_{eff}, figure 9. In the next section, these ratio will be compared to the ratio of the trace ion particle confinement time to the energy confinement time obtained within the integrated modelling framework using QuaLiKiz-JETTO.

So far we have considered collisionless plasmas. The D_i/D_e ratio with collisions is compared to the collisionless case in figure 10. The collisionality is calculated assuming $T_e = T_i = 8$ keV, $n_e = n_i = 5 \times 10^{19}$ m^{-3}. As expected, with collisions, the TEM region in terms of R/L_{T_i} range is reduced and the ITG dominated regime takes over at lower values of R/L_{T_i}, leading to D_i/D_e above unity for lower R/L_{T_i} values. Moreover, the electron–ion collisionality ν_{ei}/v^3 added to γ_k in equation (9) on the trapped electron contribution, leads to larger D_i/D_e in the ITG dominated regime.

4.2. Impact of the ion mass and charge on the ratio of ion to electron particle transport

The impact of the ion charge and mass is now investigated in the collisionless case. The weak dependence of D_i/D_e on the ion mass predicted by the analytical model of section 3,
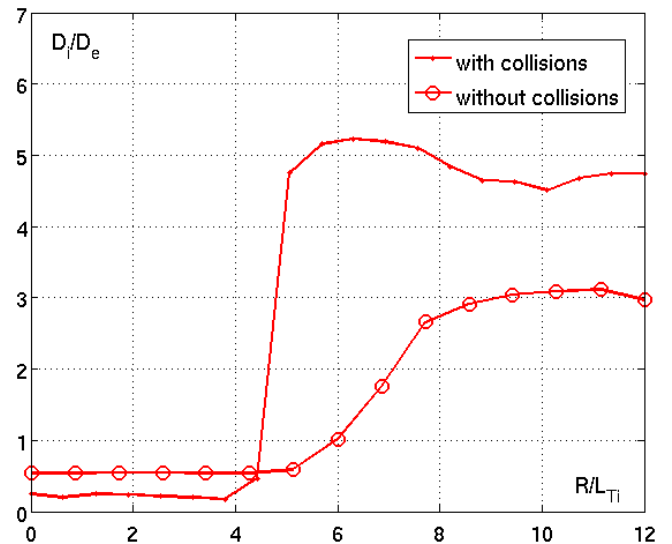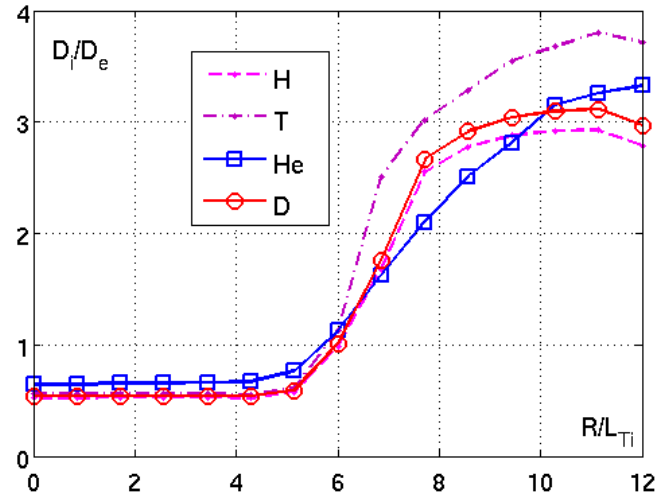
figure 4, is confirmed in QuaLiKiz simulations for H, D and T, figure 11.

Concerning trace impurities, a concentration of 10^{-5} is assumed for the various species tested: W with a mass of 184 and charge states from 0 to 40, Ne $A = 20$ $Z = 10$, Ni $A = 56$ $Z = 28$ and Kr $A = 78$ $Z = 36$. We emphasize that these calculations were carried out without rotation. In the presence of rotation, poloidal asymmetries due to the centrifugal force effectively lead to modifications of the heavy impurity convection. This effect is captured in QuaLiKiz [21, 33]. The various impurities are illustrated on figure 12 for the ITG dominated case (ITG1 see table 1) and figure 13 for the TEM dominated case (TEM1 see table 1). The W various ionisation states are plotted with full lines, Ne with diamonds, Ni with circles and Kr with squares. For both ITG and TEM dominated regimes,
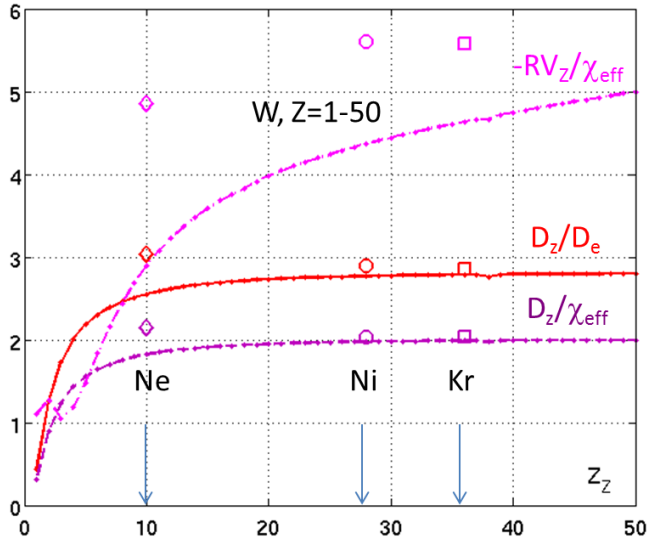
Figure 12. Ratio between the trace impurity diffusivity and 1/ the electron diffusivity (red) 2/ the effective heat diffusivity (purple), ratio between the trace impurity convective velocity (magenta) and the effective heat diffusivity versus Z_z, for the ITG1 case (see table 1). For $A_Z = 184$, corresponding to W, with a charge Z_Z varying from 1 to 50 (full lines), for Ne $A_Z = 20$ and $Z_Z = 10$ (diamonds), for Ni $A_Z = 56$ and $Z_Z = 28$ (circles) and for Kr $A_Z = 78$ and $Z_Z = 36$ (squares).
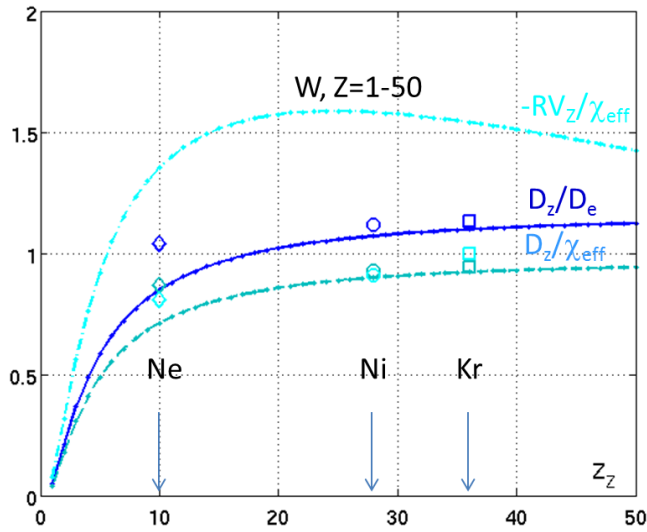

Figure 13. Ratio between the trace impurity diffusivity and 1/ the electron diffusivity (blue) 2/ the effective heat diffusivity (sky blue), ratio between the trace impurity convective velocity (cyan) and the effective heat diffusivity versus Z_z, for the TEM1 case (see table 1). For $A_Z = 184$, corresponding to W, with a charge Z_Z varying from 1 to 50 (full lines), for Ne $A_Z = 20$ and $Z_Z = 10$ (diamonds), for Ni $A_Z = 56$ and $Z_Z = 28$ (circles) and for Kr $A_Z = 78$ and $Z_Z = 36$ (squares).

the ratio of the trace impurity diffusivity to the electron diffusivity, D_Z/D_e, is only weakly affected by a mass change from 184 for W to 10 for Ni. On the contrary the charge of the trace impurity does matter, leading to larger D_Z/D_e for larger charges in both regimes as illustrated on figures 12 and 13. As for main ions, larger D_Z/D_e ratios are observed in the ITG dominated regime, while D_Z/D_e remains lower than unity for the TEM dominated case. In ITG dominated regimes, the trace
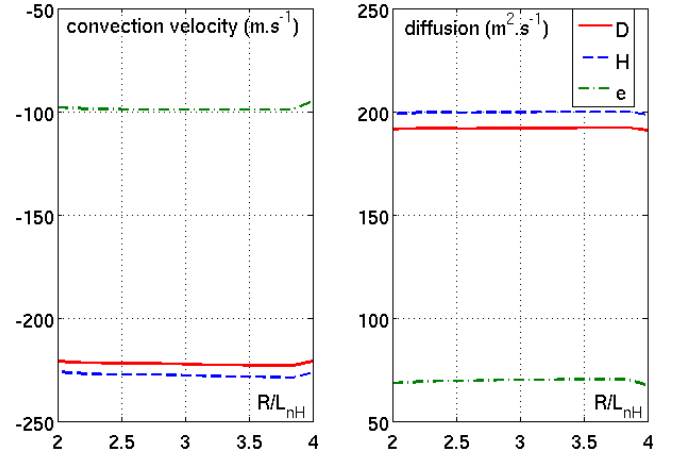

Figure 14. Convection velocity in $m.S^{-1}$ and diffusion coefficient in $m^2 \cdot S^{-1}$ are plotted with respect to R/L_{nH}. In full line, red, for D, in dashed blue line for H and in green dash-dotted line, for electrons.
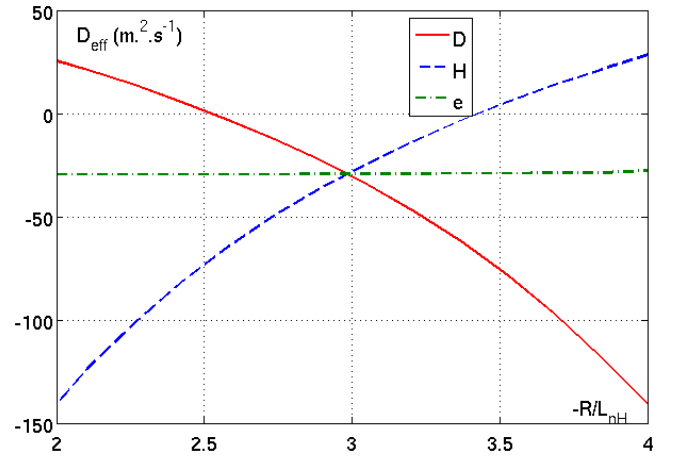

Figure 15. Effective diffusion in $m^2 \cdot S^{-1}$ plotted with respect to R/L_{nH}. In full line, red, for D, in dashed blue line for H and in green dash-dotted line, for electrons.

impurity convective contribution, directed inward, can be up to 6 times larger than the total effective diffusivity χ_{eff}. This observation could explain the observed fast impurity transport in Laser Blow Off (LBO) experiments on ASDEX Upgrade [10, 11], Tore Supra and JET [12], and CMOD [13].

4.3. Case of multiple ions

As explained in the introduction, in the case of multiple ions, the individual ion fluxes can be much larger than the electron flux, even though the total particle flux is constrained by ambipolarity.

We illustrate this point for the GA standard case (see case ITG1 in table 1) and using a plasma made of 2 ion species: D and H with a $n_D/n_e = n_H/n_e = 0.5$. The normalized density gradient of H, R/L_{nH} is varied from 2 to 4 while keeping $R/L_{ne} = 3$. R/L_{nD} is constrained by the electroneutrality, hence varies from 4 to 2.

As illustrated by figure 14, when varying R/L_{nH} at fixed R/L_{ne}, the ion transport coefficients (diffusivity and convective velocity) barely vary. Only a modification of R/L_{ne} would
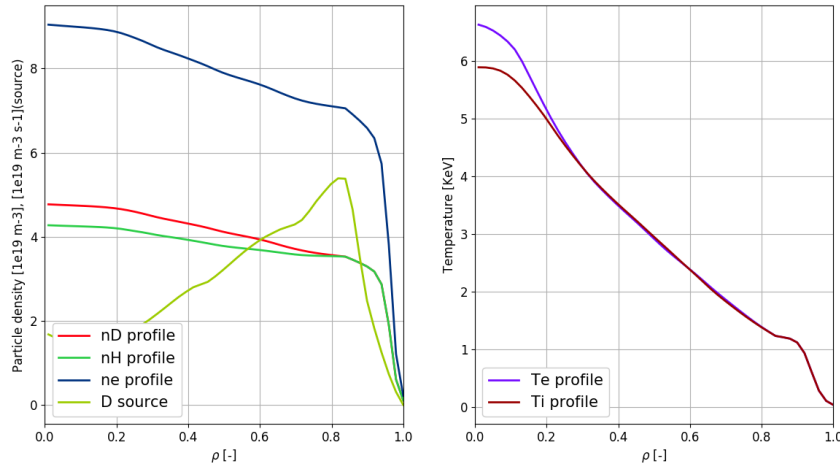
Figure 16. Relaxed density profiles for a D particle source (left panel) and ion and electron temperature profiles (right panel), for $n_H = n_D$ at $\rho = 0.85$, at 13 s.

impact significantly the ion transport coefficients. As already illustrated on figure 6, for the GA standard case (at $R/L_{Ti} = 9$), $D_D/D_e \simeq 3$ and $V_D/V_e \simeq 2.4$. And also as illustrated on figure 11, deuterium and hydrogen behave similarly with $V_D \simeq V_H$ and $D_D \simeq D_H$.

Since the ion transport coefficient values are large, the effective diffusivities, D_{eff}, defined as $D_{\text{eff}} = D + VL_n$, vary strongly with the normalized density gradient R/L_{nH} as illustrated on figure 15. The D_{eff} for deuterium and hydrogen match the electron D_{eff} for $R/L_{nD} = R/L_{nH} = R/L_{ne} = 3$ as expected.

During transient phases, in the case of multiple ions, the ion density gradients can depart from the electron density gradient. For ITG dominated cases, $|D_{\text{eff},i}|/|D_{\text{eff},e}| > 1$ is easily obtained, therefore $|\Gamma_i| > |\Gamma_e|$, leading to fast ion mixing. This will be confirmed in the next section, by studying the plasma response to a rapid change of the particle source thanks to flux driven integrated modelling simulations.

5. Integrated modelling with multiple-isotope transport

The implications of the trends explored in the previous sections are here illustrated through analysis of multiple-isotope transport dynamics within an integrated modelling framework. The transport code applied for the simulations is JETTO [22, 23], with QuaLiKiz predicting the turbulent transport. JETTO evolves the ion species, and sets the electron profile using the quasineutrality constraint. QuaLiKiz particle flux outputs are ambipolar by construction, a consequence of using the quasineutrality constraint to define the dispersion relation in the instability solver [34].

The starting point, for our numerical experiments, was the JET baseline H mode pulse #87412, previously analysed using JETTO-QuaLiKiz leading to good agreement with the experimental measurements [21]. A multiple-isotope scenario was then artificially imposed on the simulations, forcing the effective charge to be 1 and introducing an H species in the D pulse with $n_H = n_D$ in the $\rho = 0.85$–1.0 region, where ρ is the normalised toroidal flux coordinate. The electron density

profile n_e was kept as in the original discharge. Simulations with varying initial conditions were carried out, as described in the subsections below. For each case, the current and the toroidal momentum were interpretive, while electron temperature, ion temperature, H ion density and D ion density were predictive. No impurities, neutrals, or MHD (NTMs, sawteeth) were included. All NBI source calculations are from PENCIL and are peaked off-axis in this high density pulse. To simulate various regimes, the sources were artificially modified in the various cases, as described below. Neoclassical transport was calculated by NCLASS [35].

QuaLiKiz was applied in the region $0.15 < \rho < 0.85$. For the inner core at $\rho < 0.15$, where typically QuaLiKiz does not predict turbulent flux, the transport was prescribed to ensure smooth profiles towards the magnetic axis. For $\rho > 0.85$ the profiles are prescribed from the measurements.

Simulations in two separate regimes where studied. The first was the nominal regime corresponding to the actual experimental conditions, starting with an initially peaked electron density profile. All ion-scale modes were ITG dominated modes. The second regime was a TEM dominated regime. Finally, an ITG dominated regime is studied starting from a hollow density profile, this situation being more representative of an edge/SOL fuelling case.

All simulations were run for 3 s of plasma evolution, with a stationary particle source, sufficient for all profiles to converge, the energy confinement being around 95 ms for the ITG case and 46 ms for the TEM case.

5.1. ITG dominated regime, $Q_i > Q_e$

First, in D only, a stationary state for T_i, T_e and n_e was set by running JETTO-QuaLiKiz until full profile relaxation, with boundary conditions at $\rho = 0.85$ determined from averaging the experimental profiles between 10.0–10.5 s. Then, a 50–50 concentration of H and D was imposed at the $\rho = 0.85$ boundary. The NBI particle source was imposed to be pure D, and the JETTO-QuaLiKiz simulation restarted until stationary state was reached once more. The relaxed profiles are seen in figure 16. Both H and D profiles are peaked, indicating that
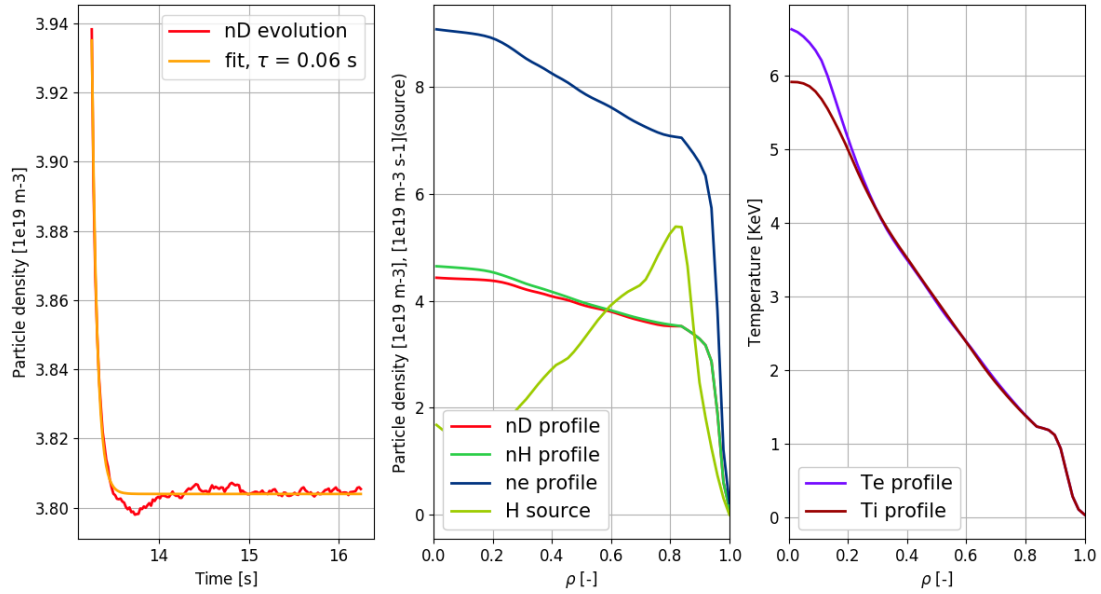
Figure 17. Evolution of the D density profile at $\rho = 0.6$ following a switch of particle source from D to H (left panel). The τ relaxation timescale is from an exponential fit. The central panel shows the final relaxed density profiles in presence of a H source, while the right panel shows the relaxed temperature profiles, at 16 s.

Table 4. Summary of the characteristic time scales for initially peaked density profiles and either ITG or TEM dominated regimes. 'Switch sources' refers to the switching from a D source to an H particle source. 'Turn off source' refers to turning off the particle source, while keeping the heating source.

	ITG dominated case		TEM dominated case	
Case	D relaxation time scale τ_D in ms	τ_D/τ_E	D relaxation time scale τ_D in ms	τ_D/τ_E
Switch sources	60	0.6	410	8.7
Turn off source	280	3.0	450	9.8

Table 5. Summary of the particle transport coefficients for the various cases, the last time-step of each simulation and at $\rho = 0.6$ ($\rho = 0.63$ for the third case due to a non representative QuaLiKiz point). D(e), D(H) and D(D) are the diffusion coefficients, in m² s⁻¹, for electrons, Hydrogen and Deuterium. Vc and Vt are the pure convective term and the thermodiffusion term, in m/s.

Case	D(e)	D(H)	D(D)	Vc(e)	Vc(H)	Vc(D)	Vt(e)	Vt(H)	Vt(D)
ITG switching D to H source	0.15	1.36	1.28	0.16	-1.33	-1.23	-0.09	0.99	0.73
ITG D source off	0.37	2.60	2.31	0.41	-2.73	-2.41	-0.31	2.78	2.20
TEM switching D to H source	7.51	3.16	2.33	-5.40	-0.42	-0.67	-2.36	-1.91	-2.12
TEM D source off	5.13	0.81	0.50	-3.24	-0.12	-0.17	-2.33	-0.67	-0.50
Hollow H profile	0.18	1.57	1.38	0.19	-1.51	-1.32	-0.16	1.28	0.98

Table 6. Summary of the particle fluxes and effective particle diffusivities for the various cases, at the last time-step of each simulation and at $\rho = 0.6$. $\Gamma_{e,H,D}$ are the particle fluxes, normalized to 1×10^{19}, in m⁻² s⁻¹, for electrons, Hydrogen and Deuterium. $D_{\text{eff},e,H,D}$ are the effective diffusion coefficients, in m² s⁻¹. Zero flux and D_{eff} corresponds to zero source for that species.

Case	Γ_e	$D_{\text{eff},e}$	Γ_H	$D_{\text{eff},H}$	Γ_D	$D_{\text{eff},D}$
ITG switch D to H source	0.87	0.28	0.87	0.55	0.0	0.0
ITG all source offs	0.0	0.0	0.0	0.0	0.0	0.0
TEM switch D to H source	0.63	0.42	0.63	0.91	0.0	0.0
TEM all sources off	0.0	0.0	0.0	0.0	0.0	0.0
Hollow H profile	0.56	0.30	0.0	0.0	0.56	0.43

Table 7. Summary of the particle heat fluxes and effective thermal diffusivities for the various cases, averaged on the last 400 ms of each run, $\rho = 0.6$. $Q_{e,i}$ are the heat fluxes, in kW m⁻². $\chi \text{eff}_{e,i}$ are the effective thermal diffusivities, in m² s⁻¹. For the ions we state the averaged value. The individual isotope thermal diffusivities are very similar.

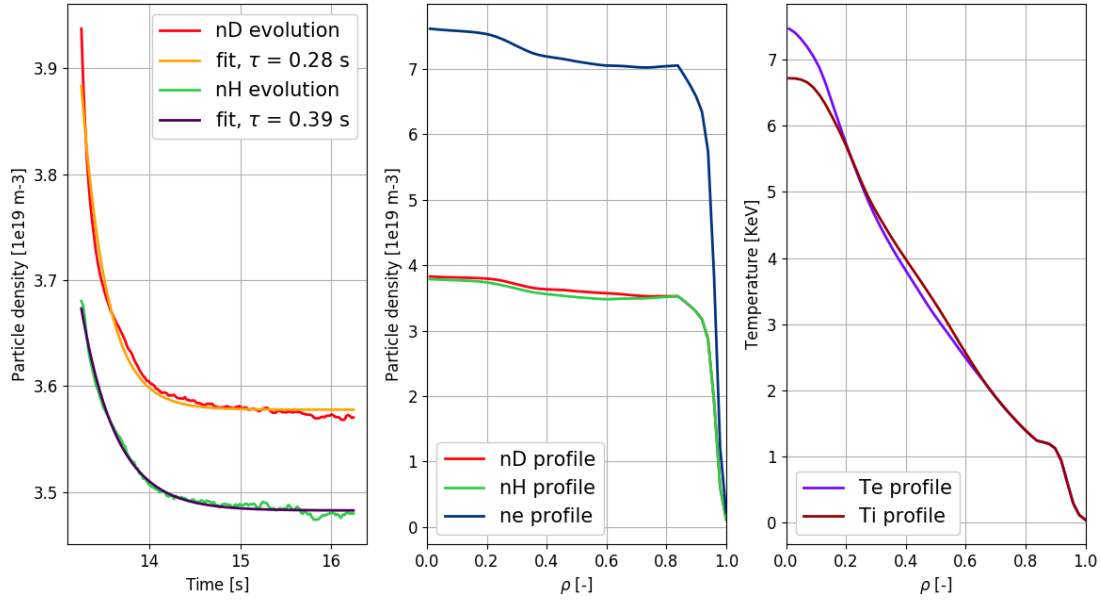| Case	Q_e	Q_i	$\chi_{\text{eff},e}$	$\chi_{\text{eff},i}$
ITG switching D to H source	39.7	116.5	0.61	1.63
ITG D source off	52.6	106.6	0.72	1.21
TEM switching D to H source	92.4	5.84	2.48	1.15
TEM D source off	89.4	4.70	2.00	0.52
Hollow H profile	36.7	112.5	0.67	1.93

Figure 18. Evolution of n_e and n_D at $\rho = 0.6$ after turning off all particle sources (left panel). The final relaxed density profiles are shown in the central panel, the final temperature profiles are shown in the right panel, at 16 s.
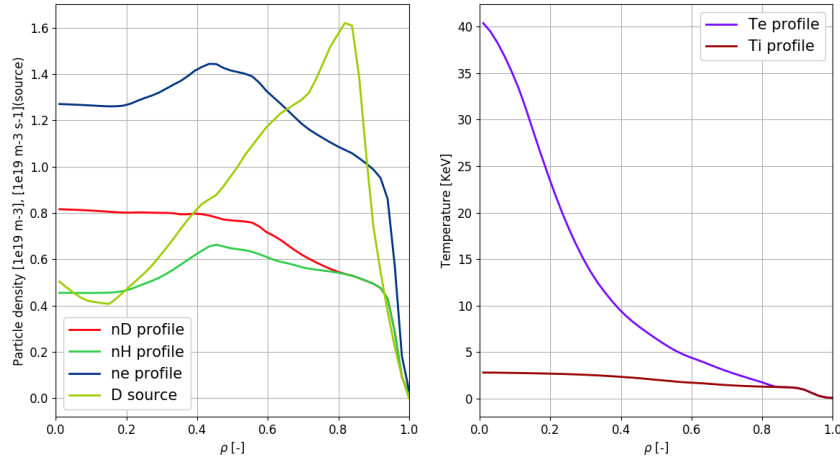

Figure 19. Simulation of a prescribed TEM dominated regime, with a D particle source and both H and D isotopes. The final states of the densities are shown in the left panel. The temperature profiles are shown in the right panel at 13 s.

both D and H profiles are controlled by the large D_i and an inward V_i. The large D_i reducing the source impact on the final profiles as discussed earlier, see equation (6).

We then proceed to separate the ion and electron particle confinement timescales.

In the first case, the NBI D particle source was switched to a H particle source. The H and D profiles evolved during the 3 s simulation time, while the electron density remains mostly unchanged. The D profile evolution at $\rho = 0.6$ can be seen in figure 17 (left panel). The final density profiles for D, H and electrons in figure 17 (central panel) and the final T_i and T_e (right panel) are similar to the initial ones figure 16.

The similitude observed between a D particle source (figure 16) and a H particle source figure 17 was expected from the QuaLiKiz stand alone analysis of section 4, where it was shown on figure 11 and on figure 14, that D_i/D_e, D_i and V_i are similar for H and D.

The D relaxation timescale was determined to be $\tau = 0.06$ s following an exponential fit, i.e. faster than the energy confinement time, see table 4. See table 5 for the detailed values of D_e, D_i, V_{te}, V_{ti}, V_{ce}, V_{ci} at the end of the simulation, tables 6 and 7 for the heat and particle fluxes.

In the second case, starting from the profiles of figure 16 at 13 s, all particle sources were turned off to identify the timescale of electron particle transport. The results are shown in figure 18, with the left panel corresponding to the decay of n_e, n_H and n_D at $\rho = 0.6$, and the final relaxed density profiles shown in the central panel. On the right panel one sees that T_i and T_e slightly increase as a result of the density decrease. The decay of D, H and n_e perfectly coincide, since the evolving electrons control the isotope transport. As expected from previous sections, this timescale is around 5 times slower than in the isotope mixing case, with $\tau = 0.28$ s and slower than the energy confinement time, see table 4 for a summary of the time scales and table 5 for a
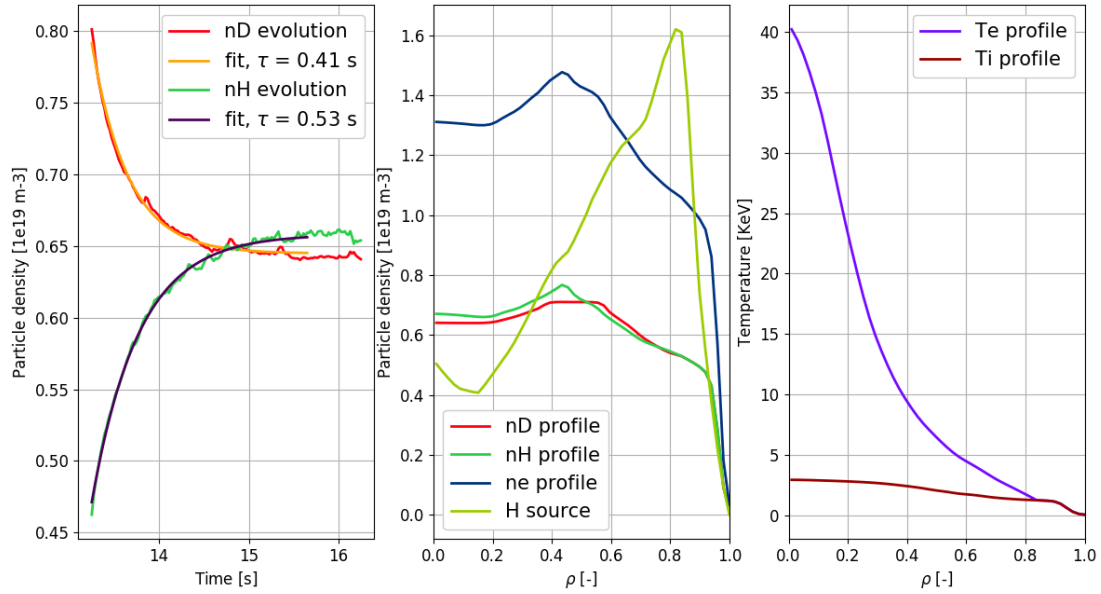
Figure 20. TEM dominated regime. Evolution of D and H density at $\rho = 0.6$ when exchanging the particle source from D to H (left panel), relaxed final densities in presence of a H source (central panel) and temperature profiles (right panel) at 16 s.
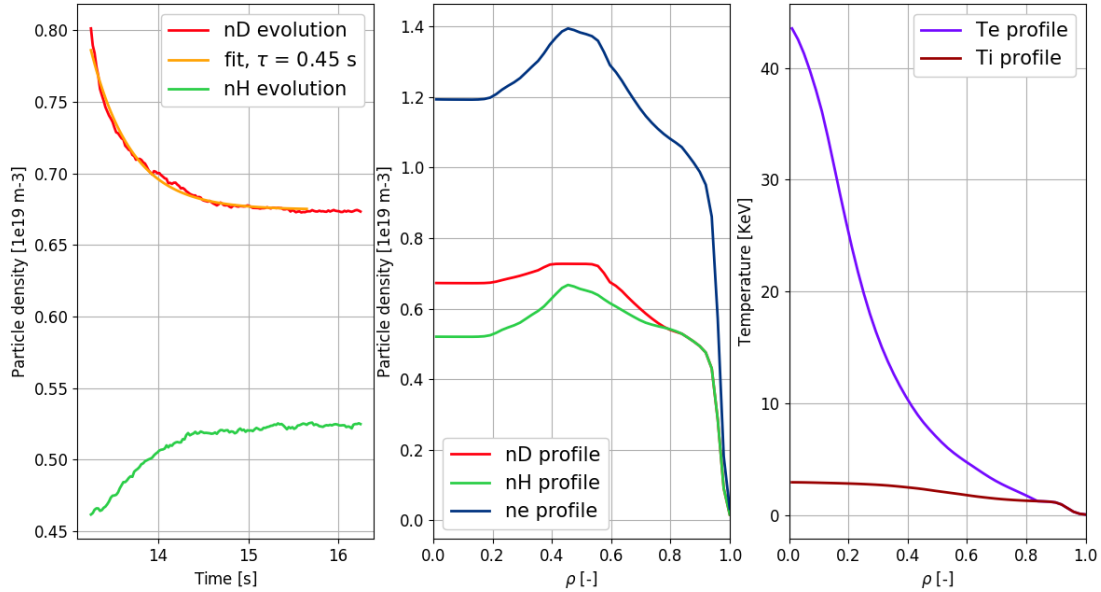

Figure 21. TEM dominated regime. Evolution of D and H density at $\rho = 0.6$ when turning off the particle source (left panel). Relaxed density (central panel) and temperature (right panel) profiles at 16 s.

summary of the diffusion and convection coefficients. It is also interesting to note that the final electron density profile, without source, is slightly flatter than the initial one with an off-axis source. Finally, we note that even though JETTO only evolves the ions (and sets n_e through quasineutrality), the slower ion transport in this case is caused by the time-dependent impact of the evolving R/L_{ne} on the ion transport coefficients.

5.2. TEM dominated regime, $Q_e \gg Q_i$

In a TEM dominated regime, the starting point was the pulse #87412, but with prescribed reduced density to reduce the

collisionality and increase the TEM drive. Furthermore, the heating power was forced to only heat the electrons and reach a TEM dominated regime. The same numerical experiments were carried out: exchanging the D particle source to a H source and switching off the particle source.

The final stationary states of the mixed-isotope simulation with a D particle source, are shown in figure 19. It is striking that, in the TEM dominated case, as opposed to the ITG dominated case, there are significant differences in the isotope profiles and the source location impacts the density profile shape. In figure 20, when exchanging the D source to a H source, we find an isotope remixing time of $\tau \approx 0.3$ s, significantly slower than the analogous simulation in the ITG dominated
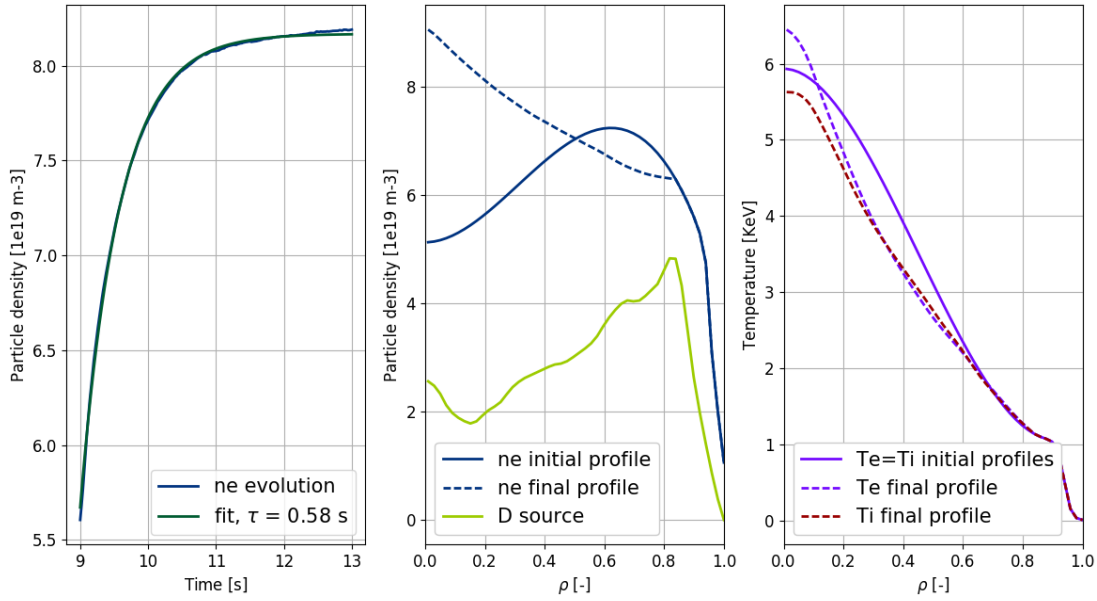
Figure 22. The n_e (and thus n_D) evolution at $\rho = 0.2$ is shown in the left panel. The electron density initial and final profiles for the hollow-to-peaked transition are shown in the central panel, the particle source profile is also displayed. The right panel shows the initial and final temperature profiles.
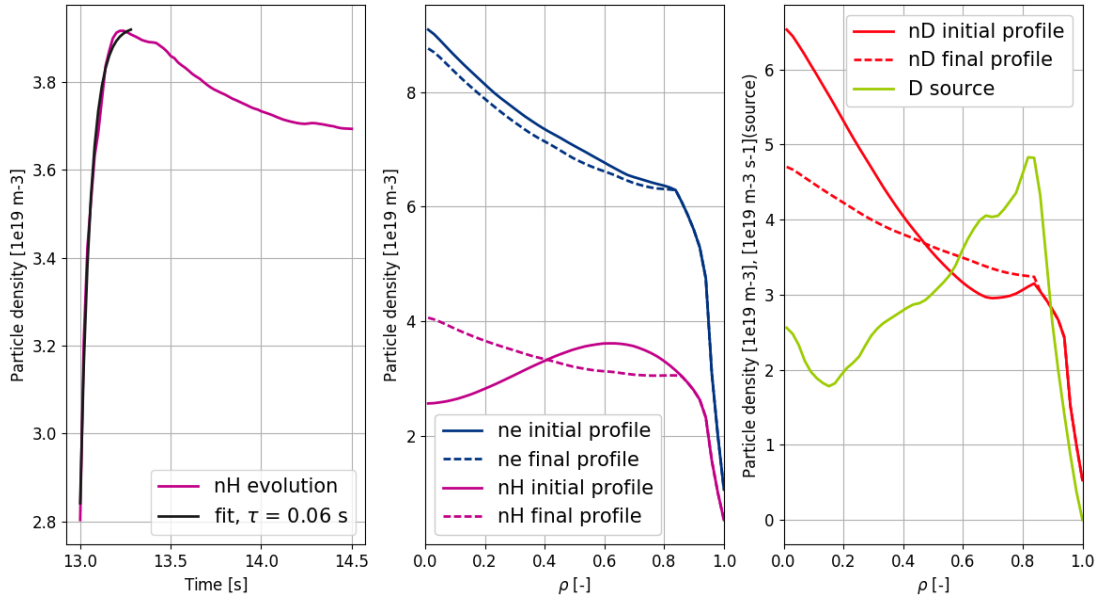

Figure 23. The time evolution and fitted relaxation timescale of n_H at $\rho = 0.2$ is shown in the left panel. In the central panel, the initial and final n_e profiles and the initial and final n_H profiles are shown. The right panel shows the D particle source, as well as the initial and final n_D profiles.

case see also table 4, due to lower D_i and V_i in the TEM dominated case as detailed in table 5.

When the particle source is removed, figure 21, the time scale needed for the D profile to relax to a new shape is $\tau \approx 0.47$ s. This time is comparable to the isotope mixing time. Moreover, we do not have significantly faster electron particle transport in the TEM dominated regime compared to the ITG dominated regime, see the characterisitic time scales summarized in table 4 and the diffusive and convective coefficients summarized in table 5. This is consistent with the analytical findings in section 3 showing that the passing ions can still provide significant transport in a TEM regime.

5.3. ITG dominated regime, $Q_i > Q_e$. Hollow density profiles

Of relevance to core fuelling is the timescale of isotope mixing starting from a hollow density profile, e.g. following a gas puff or pellet injection. To analyse this, the starting point is now the measured #87412 kinetic profiles at 9 s, corresponding to the time directly following the L to H transition where the initial n_e profile is hollow, see figure 22. To compare isotope and electron transport timescales two numerical experiments are carried out. First the hollow electron density profile evolves, with a D source and D only, until it reaches a stationary peaked state, see figure 22. The left plot displays

the initial and final n_e profiles of the simulation, with the n_e evolution at $\rho = 0.2$ shown in the right plot. The timescale for the filling in and relaxation of the n_e profile was $\tau_e = 0.58$ s. Similar slow time scales were found in JET high I_p off-axis particle source experiments [36] and in the associated CRONOS-QuaLiKiz modelling [37].

In a second numerical experiment, a n_H profile with an initial hollow profile similar to the initial n_e illustrated on figure 22(*a*) was added to the system. The boundary condition at $\rho = 0.85$ was set to $n_H = n_D$. The electron profile was left unchanged (the final profile from figure 22(*a*)), and the D profile was adjusted to match quasineutrality. The simulation was restarted, and the relaxation time of the system then corresponds to the H isotope relaxation time, evolving from hollow to peaked. The results are shown in figure 23. As expected, an evolution for the isotope mixing an order of magnitude faster than the electron hollow-to-peaked time was observed: $\tau_H = 0.057$ s, see also table 5 where the electrons, D and H transport coefficients are reported. Note that two timescales are evident in figure 23. The fast timescale of the major evolution of H, and then a slower timescale corresponding to the correction due to a minor evolution of n_e which then impacts the n_H profile as well.

6. Conclusion

Thanks to a comprehensive approach including nonlinear gyrokinetic modelling, analytical derivation, quasilinear modelling and integrated source driven modelling, we have demonstrated that ion particle transport coefficients differ significantly from electron particle transport coefficients while respecting ambipolar fluxes.

In the case of dominant ITG turbulence (i.e. $Q_i > Q_e/2$), ratios of the ion to electron diffusive and convective terms up to 5 are obtained. The resonance condition, in the case of ITG dominated turbulence, leads to both larger ion heat fluxes as well as larger ion particle diffusive and convective coefficients. This dependence of D_i/D_e on the resonance condition is strongly related to the well known result that ion heat flux dominates electron heat flux for ITG dominated regimes, and electron heat flux is dominant for TEM regimes. In the present work on the particle flux ratio, the results are obtained in fixed gradient nonlinear gyrokinetic simulations using GKW [19] for D, are derived in the quasilinear analytical limit for H isotopes and heavier ions, and confirmed with QuaLiKiz [38], for H isotopes and impurities, where the quasilinear particle diffusivities for D are very close to the nonlinear results for both ITG and TEM dominated cases.

During transient phases, in the case of multiple ions, the ion density gradients can depart from the electron density gradient. For ITG dominated cases, $|D_{\mathrm{eff,i}}|/|D_{\mathrm{eff,e}}| > 1$ are easily obtained, therefore $|\Gamma_i| > |\Gamma_e|$, leading to fast ion mixing. This is confirmed by JETTO-QuaLiKiz [21] source driven numerical experiments, for JET-like ITG dominated regime, similar H and D density profiles are obtained independently of the nature of the ion core particle source (i.e. either H or D). The isotope mixing time is around 60 ms whereas the electron particle transport time is more than 4 times larger at 280 ms. The situation reverses in the case of TEM dominated turbulence (i.e. $Q_e > 2 \times Q_i$), where $D_i < D_e$ and $V_i < V_e$ are obtained and where the ion mixing time is of the same order of the electron particle transport time (resp. 410 ms and 450 ms).

In tokamaks, in presence of sufficient ion heating such that $Q_i > Q_e/2$, dominant ITG regime is often encountered. $Q_i > Q_e/2$ is also expected in reactor-relevant high density plasmas where the ion–electron heat exchange and radiation contributions play a significant role [28, 29, 31, 32].

Our findings are consistent with numerous experimental observations: similar H and D density profiles in JET-ILW in presence of core D source [6], very fast trace T transport in TFTR [3], fast trace He transport in DIII-D D plasmas [7], and laser blow off of impurities showing impurity transport times significantly larger than the energy confinement time [12, 13].

The next steps are to apply QuaLiKiz-JETTO for modelling recent mixed isotope scenarios in JET, in preparation for DT operation, as well as previous laser blow off experiments. ITER scenarios will then be addressed focusing on isotope mixing, He ash transport, edge fuelling, and impurity contamination in H, He and DT scenarios.

Acknowledgment

Appendix

The quasilinear approach and justifications thereof are summarized in [20, 21, 38, 39, 40] and references therein. The quasilinear particle flux is defined as $\Gamma_s = \langle \delta n_s \delta V_{E\times B} \rangle$, where $\langle \dots \rangle$ is a flux surface average and time average over τ, an intermediate timescale $1/\gamma < \tau < T_0$, where T_0 is the equilibrium (transport) timescale and γ the linear growth rate. For electrostatic turbulence using the linearized Vlasov equation, the particle flux for a given mode k can be expressed as the product of a linear plasma response with a saturated electrostatic potential as follows:

$$\Gamma_{ks} = \mathrm{Re}\langle \delta n_s \frac{\mathrm{i}k_\theta \delta\phi}{B} \rangle$$
$$\simeq -\langle k_\theta \frac{f_0^s e_s}{B T_s} \mathrm{Im} \frac{n\omega_s^* - n\omega_{d,s} - k_\parallel v_{\parallel,s}}{\omega_k - n\omega_{d,s} - k_\parallel v_{\parallel,s} + \mathrm{i}0^+} |\phi_k|^2 \rangle_{\epsilon,\lambda,\theta} \tag{A.1}$$

where the integration is over velocity space (energy and pitch angle) and flux surface. ω_k is the real part of the

eigenfrequency calculated from the dispersion relation defined by the weak formulation of the quasineutrality constraint $\langle \sum_s q_s \delta n_s \phi_k \rangle = 0$. This constraint also ensures intrinsic ambipolarity for each mode, as defined by $\sum_i Z_i \Gamma_{ki} = \Gamma_{ke}$. $n\omega_{ds}$ is the ∇B and curvature drift:

$$n\omega_{ds} \simeq -\frac{k_\theta T_s}{e_s BR}\mathcal{E}(2 - \lambda b(\theta)) \tag{A.2}$$

where e_s is the species charge, B the magnetic field, R the major radius, λ is the pitch angle at the low-field-side (LFS), and $b(\theta)$ the poloidally dependent modification of the pitch angle due to the magnetic mirror effect. $\mathcal{E}$ is the particle energy normalised to the species temperature. The parallel dynamics term is:

$$k_\| v_{\|,s} \simeq k_\theta x \frac{\hat{s}}{q}\frac{v_{ths}}{R}\sqrt{\mathcal{E}}. \tag{A.3}$$

Where q is the safety factor, $\hat{s}$ the magnetic shear, x is the distance from the central flux surface of the mode, and $v_{ths} \equiv \sqrt{2T_s/m_s}$ the thermal velocity. The diamagnetic frequency $n\omega_s^*$ due to gradients with respect to the equilibrium Maxwellian f_0 is:

$$n\omega_s^* = -k_\theta \frac{T_s}{e_s BR}\left(\frac{R}{L_{n_s}} + \left(\mathcal{E} - \frac{3}{2}\right)\frac{R}{L_{T_s}}\right) \tag{A.4}$$

where we have ignored rotation effects, and $L_{n_s} \equiv -\frac{\nabla n_s}{n_s}$, $L_{T_s} \equiv -\frac{\nabla T_s}{T_s}$. We have defined the negative direction as the ion diamagnetic direction.

Nonlinear effects broaden the frequency spectrum, hence a finite value will be used instead of 0^+ in equation (A.1). It has been shown that for low-k modes which drive the majority of the transport, the frequency spectrum can be represented by a Lorentzian whose width is of the order of γ_k, the imaginary part of the solution of the dispersion relation (i.e. the growth rate). This assumption has been shown to be valid over a large range of parameters [39, 40], and we apply it here henceforth. Note that energy, and momentum transport fluxes are similarly derived [41, 42].

We now make the following significant approximations to reduce equation (A.1) into an easily calculable form maintaining the key physics setting the D_i/D_e and V_i/V_e ratios.

- Remove spatial dependence by focusing on the outboard midplane and setting $\theta = 0$. Hence $b(\theta) = 0$ in equation (A.2), and ϕ_k becomes a scalar. We also set an average $x \approx d$, where $d = 1/\hat{s}k_\theta$ is the distance between neighbouring flux surfaces. This sets $k_\| \approx 1/qR$
- Simplify the velocity space integration by assuming all passing particles have pitch angle $\lambda = 0$, and all trapped particles have $\lambda = 1$. The pitch angle integration then simply extracts the trapped and passing particle fractions
- Bounce average the trapped particles, which then removes the parallel dynamics term for trapped particles (on average $v_\| = 0$)
- Neglect impact of collisions on the quasilinear response, and assume $T_s = T$ for all particle species
- Take a drift kinetic limit and neglect finite Larmor radius effects

Following these approximations, we can split the contribution of the particle flux of each species, for a given mode k, by trapped Γ_{ts} and passing particles Γ_{ps}, as follows:

$$\Gamma_{ts} \propto f_t \left\langle \frac{\frac{R}{L_{n_s}} + \left(v^2 - \frac{3}{2}\right)\frac{R}{L_{T_s}} - v^2}{\left(\bar{\omega}_k + \frac{k_\theta \rho_0}{Z_s}v^2\right)^2 + \bar{\gamma}_k^2} \right\rangle \tag{A.5}$$

$$\Gamma_{ps} \propto f_p \left\langle \frac{\frac{R}{L_{n_s}} + \left(v^2 - \frac{3}{2}\right)\frac{R}{L_{T_s}} - 2v^2 + \frac{Z_s}{q}\sqrt{\frac{2m_p}{m_s}}\frac{v}{k_\theta \rho_0}}{\left(\bar{\omega}_k + \frac{2k_\theta \rho_0}{Z_s}v^2 - \frac{1}{q}\sqrt{\frac{2m_p}{m_s}}v\right)^2 + \bar{\gamma}_k^2} \right\rangle \tag{A.6}$$

where $v^2 \equiv \mathcal{E}$, $f_{t,p}$ are the trapped and passing fractions respectively, and $\langle \cdot \rangle$ here represents integration over v: $\int_{-\infty}^{\infty} v^2 e^{-v^2}\mathrm{d}v$. Both Γ_t and Γ_p share the same proportionality constant. $\rho_0 \equiv \frac{\sqrt{Tm_p}}{eB}$ is the Larmor radius with respect to the proton sound speed $c_s = \sqrt{T/m_p}$, where m_p is the proton mass. $\bar{\omega}_k$ and $\bar{\gamma}_k$ correspond to normalization by c_s/R.

The particle flux Γ_s can be decomposed as:

$$\Gamma_s = -D_s\frac{\mathrm{d}n_s}{\mathrm{d}r} + (V_{t,s} + V_{c,s})n_s. \tag{A.7}$$

For a review on particle transport and the various convective terms see [1, 27]. D_s is the diffusion term, $V_{t,s}$ is the thermodiffusion convective velocity, and $V_{c,s}$ is the pure convective velocity. From equations (A.5)–(A.6), it is clear that D_s arises from the term proportional to $\frac{R}{L_n}$ in $n\omega_s^*$, V_t from the term proportional to $\frac{R}{L_T}$ in $n\omega_s^*$, and V_c from the terms proportional to the ∇B drift frequency and parallel dynamics term. Here we neglect rotation, hence the rotodiffusion.

References

[1] Angioni C. *et al* 2009 *Plasma Phys. Control. Fusion* **51** 124017
[2] Fable E. and Angioni C. 2010 *Plasma Phys.* **52** 015007
[3] Efthimion P.C. *et al* 1995 *Phys. Rev. Lett.* **75** 85
[4] Zastrow K.-D. *et al* 2004 *Plasma Phys. Control. Fusion* **46** B255
[5] Valovic M. *et al* 2017 *ITPA Transport and Confinement (Princeton, May 2017)*
[6] Maslov M. *et al* 2018 *Nucl. Fusion* **58** 076022
[7] Wade M.R. *et al* 1995 *Phys. Plasmas* **2** 2357
[8] Angioni C. *et al* 2009 *Nucl. Fusion* **49** 055013
[9] Estrada-Mila C., Candy J. and Waltz R.E. 2005 *Phys. Plasmas* **12** 022305
[10] Dux R. *et al* 2003 *Plasma Phys. Control. Fusion* **45** 1815–25
[11] Angioni C. *et al* 2007 *Plasma Phys. Control. Fusion* **49** 2027
[12] Mattioli M. *et al* 1995 *Nucl. Fusion* **35** 1115
[13] Howard N.T. *et al* 2012 *Nucl. Fusion* **52** 063002
[14] Angioni C. and Peeters A.G. 2006 *Phys. Rev. Lett.* **96** 095003
[15] Angioni C. *et al* 2007 *Phys. Plasmas* **14** 055905
[16] Casson F. *et al* 2013 *Nucl. Fusion* **53** 063026
[17] Angioni C. *et al* 2015 *Phys. Plasmas* **22** 055902
[18] Angioni C. 2015 *Phys. Plasmas* **22** 102501
[19] Peeters A.G., Camenen Y., Casson F.J., Hornsby W.A., Snodin A.P., Strintzi D. and Szepesi G. 2009 *Comput. Phys. Commun.* **180** 2650

[20] Bourdelle C., Garbet X., Imbeaux F., Casati A., Dubuit N., Guirlet R. and Parisot T. 2007 *Phys. Plasmas* **14** 112501

[21] Citrin J. *et al* 2017 *Plasma Phys. Control. Fusion* **59** 124005

[22] Cenacchi G. and Taroni A. 1988 *JETTO: a Free-Boundary Plasma Transport Code* JET-IR (https://inis.iaea.org/search/search.aspx?orig_q=RN:19097143)

[23] Romanelli M. *et al* 2014 *Plasma Fusion Res.* **9** 3403023

[24] Waltz R., Kerbel G.D. and Milovich J. 1994 *Phys. Plasmas* **1** 2229

[25] Mikkelsen D.R. *et al* 2015 *Phys. Plasmas* **22** 062301

[26] Miller R.L., Chu M.S., Greene J.M., Lin-Liu Y.R. and Waltz R.E. 1998 Noncircular, finite aspect ratio, local equilibrium model *Phys. Plasmas* **5** 973

[27] Angioni C., Camenen Y., Casson F., Fable E., McDermott R., Peeters A.G. and Rice J. 2012 *Nucl. Fusion* **52** 114003

[28] Fable E., Wenninger R. and Kemp R. 2017 *Nucl. Fusion* **57** 022015

[29] Fable E. 2017 private communication

[30] Kim J.Y. and Han H.S. 2017 *Phys. Plasmas* **24** 072501

[31] Militello-Asp E. *et al* 2016 *Preprint: 2016 IAEA Fusion Energy Conf. (Kyoto, Japan, 17–22 October 2016)* (https://conferences.iaea.org/indico/event/98/session/20/contribution/255)

[32] Koechl F. 2018 private communication

[33] Angioni C. *et al* 2012 *Phys. Plasmas* **19** 122311

[34] Waltz R.E., Casati A. and Staebler G.M. 2009 *Phys. Plasmas* **16** 072303

[35] Houlberg W.A., Shaing K.C., Hirshman S.P. and Zarnstroff M.C. 1997 *Phys. Plasmas* **4** 3230

[36] Loarte A. *et al* 2013 *Nucl. Fusion* **53** 083031

[37] Baiocchi B., Bourdelle C., Angioni C., Imbeaux F., Loarte A., Maslov M. and JET Contributors 2015 *Nucl. Fusion* **55** 123001

[38] Bourdelle C., Citrin J., Baiocchi B., Casati A., Cottier P., Garbet X., Imbeaux F. and JET EFDA contributors 2016 *Plasma Phys. Control. Fusion* **58** 014036

[39] Casati A. *et al* 2009 *Nucl. Fusion* **49** 085012

[40] Citrin J., Bourdelle C., Cottier P., Escande D.F., Guercan O.D., Hatch D.R., Hogeweij G.M.D., Jenko F. and Pueschel M.J. 2012 *Phys. Plasmas* **19** 062305

[41] Cottier P., Bourdelle C., Camenen Y., Gürcan O.D., Casson F.J., Garbet X., Hennequin P. and Tala T. 2014 *Plasma Phys. Control. Fusion* **56** 015011

[42] Bourdelle C. 2015 *Habilitation à Diriger des Recherches* (Aix-Marseille University) (https://tel.archives-ouvertes.fr/tel-01113299/)

[43] Litaudon X. *et al* 2017 *Nucl. Fusion* **57** 102001